Three-dimensional spintronic devices

Luka Skoric

NanoDTC Midi Project Report

PIs: Dr Amalio Fernández-Pacheco, Dr Hannah Joyce
Daily supervisors: Dedalo Sanz Hernandez, Sarwat Baig

August 11, 2017

Declaration: "This report is substantially my own work and conforms to the University of Cambridge's guidelines on plagiarism. Where reference has been made to other research or work done by me in collaboration with others, this is clearly acknowledged in the text, bibliography and acknowledgements."

Abstract

Spintronic technologies have a great potential to substitute CMOS in the coming future, leading to low-power nanoelectronic architectures. In particular, the development of 3D spintronic memory and logic devices could have a revolutionary impact. However, there are great fabrication and characterisation challenges in implementation of 3D nanostructures. In this project, work has been done towards optimisation of focused electron beam induced deposition for fabrication of out-of-plane magnetic nanowires and streamlining the structure design process. Simple nanowires were created and the domain wall motion along their length characterised via dark-field MOKE technique recently developed by the AFP group. Work has been done towards electrical contacting of 3D nanostructures from the top, an important step for characterisation of magneto-electrical properties. For this purpose, a fabrication process using parylene as a spacer layer has been investigated. It was shown that parylene can be used as the spacer layer while still allowing for magneto-optical characterisation. This project was based on an active collaboration between the Thin Film Magnetism group at the Cavendish Laboratory and the Electronic Devices and Materials group at the Department of Engineering.

Contents

1 Introduction

Spintronics is an area of Physics which investigates solid-state physics of intrinsic electron spin and its associated magnetic moment for applications in sensing, information storage and processing. Memory and logic devices based on domain wall (DW) motion along magnetic nanowires (NWs) [1, 2] are one of the most advanced non-volatile spintronic systems ever realised. NWs can exploit shape anisotropy to store long data sequences by breaking them into domains of largely uniform magnetisation, parallel or antiparallel to the direction of the wire, separated by a well defined DWs. These domains can be propagated with external magnetic fields or current pulses throughout the NW in a shift register scheme. Bits flowing along nanowire act as a collection of separated packets able to perform logic operation making the wire not a mere inter-connector, but a device itself.

1.1 Domain walls in nanowires

Domain walls in nanostrips and nanowires offer a wealth of fascinating physical phenomena which has attracted a great deal of scientific attention [2, 3, 4]. The DW size and shape can vary greatly depending on the type and topology of the magnetic material. Single-layered magnetic nanostrips have an in-plane

magnetisation due to a large vertical shape anisotropy with DWs in three possible configurations. These can be tuned by thickness and width of the magnetic layer. In wide and thick layers, vortex walls are energetically favoured. However, when confined symmetric to smaller regions, symmetric transverse, and asymmetric transverse walls can arise [5]. Carefully constructed multilayered materials can lead to perpendicular anisotropies providing additional DW topologies such as Bloch and Neel walls [6]. If deposited over a material with high spin-orbit coupling (e.g. platinum), DWs in these materials can be tightly packed and efficiently moved with current pulses with velocities of over 350ms^{-1} [2].

The controlled domain wall motion by application of appropriate external magnetic fields or electric currents, together with their injection and trapping has been studied in recent years [7, 8]. It has been demonstrated that using the aforementioned effects, the DW-based devices with simple architectures are able to perform a complete set of logic operations [1]. In addition, the appearance of unexpected effects such as spin-orbit torques in highly-asymmetric systems due to Dzyaloshinskii-Moriya interactions (DMI) [9] and chiral symmetry breaking resulting in formation of skyrmionic vortices [10] have a potential to greatly increase the efficiency and speed of domain wall motion, offering a range of phenomena that are still being explored for applications in technology.

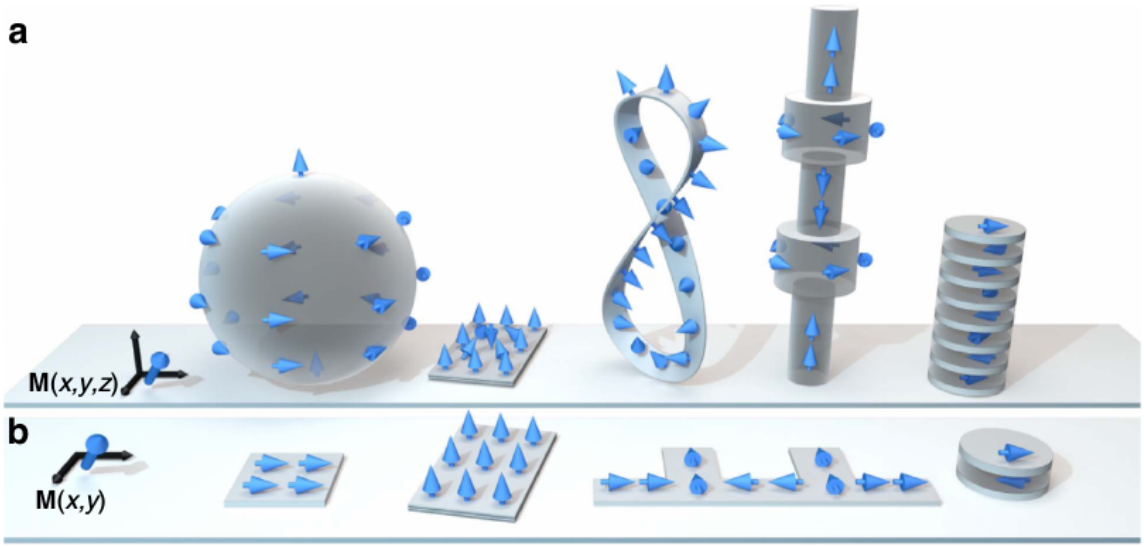

Figure 1: Towards 3D Spintronics. New synthesis, characterisation and computational methods have a potential to make a leap to 3D. The emergence of unexplored physical phenomena in these systems, due to complex magnetic states and additional degrees of freedom, may find applications in multiple areas. Until now, most works have been dedicated to nanostrips, i.e. 2D nanowires on the substrate plane. Adapted from [3]

1.2 3D spintronics

Simulations of three dimensional systems such as spirals, tubes and spheres suggest the emergence of unexplored physics [3, 4]. Different geometries lead to new types of domain walls, such as transverse-vortex and Bloch-point walls, additional pinning potentials, and chirality dependent DW motion. Moreover, recent theoretical results predict that the breaking of chiral symmetry can induce strong DMI-like effects [11] increasing the attainable density of DWs.

The concepts for 3D spintronic devices, such as the "racetrack memory" [2] and skyrmionic bubble memories [12] have been developed. These have a potential to become a disruptive technology outperforming CMOS by having storage capacities reaching Tbit/in^2, non-volatility, low power consumption during operation, and with the ability of performing logic operations. However, so far, very few of such systems have been experimentally realised due to huge challenges regarding fabrication and characterisation of three-dimensional nanostructures. This has been restricting the memory density of spintronic devices when compared to modern CMOS architectures, limiting their technological applicability.

New nano-printing methods [13, 14] make now possible, for the first time, the development of 3D magnetic nanostructures (Fig. 1). 3D geometries opens routes to explore new physics, impacting areas such as data storage, sensing and nanoelectronics. In particular, in the field of spintronics, the creation of nanowires with non-planar configuration are suitable to explore recently-predicted dynamical effects in

new types of DWs. They also would allow to control unexplored sources of anisotropy and antisymmetric exchange interactions.

1.3 Previous work

The advances in three-dimensional DW devices are expected to open a fascinating new chapter in the spintronic area. The TFM group is a pioneer in this area [3], including nanofabrication, advanced characterisation of 3D magnetic nanostructures [13, 14], and development of new concepts for spintronic applications [15, 16].

In particular, dark field Magneto-Optical Kerr effect (MOKE) setup was recently developed for the purpose of characterisation of magnetic properties of out-of-plane nanowires [17]. Moreover, a collaboration has been established with J.D.Fowlkes at the Center for Nanophase Materials Sciences (CNMS) in order to use their recently developed simulations and expertise in 3D FEBID nanoprinting [18, 19].

The Joyce group has expertise in creating electrical contact and characterisation of electrical properties of vertically grown nanowires [20, 21]. In this project, we decided to work on using their recently developed method for top contact fabrication using parylene as the spacer layer.

This project was divided into three main sections: FEBID 3D nanoprinting, magneto-optical characterisation and electrical contacting. Firstly, I worked towards furthering the group's knowledge on 3D nanofabrication in order to get a reliable growth of simple nanostructures as a step of going towards complex geometries. Secondly, I have applied optical characterisation methods on built structures to characterise domain wall injection and motion. Finally, I worked towards developing the lithography techniques for top contact fabrication which would allow us to electrically characterise the nanostructures.

2 3D nanoprinting

2.1 Overview

Focused Electron Beam Induced Deposition (FEBID) is a direct-writing deposition technique which has been receiving a strongly increasing attention in the last decade [22, 23, 24, 18]. The resolutions going down to 3 nm in SEMs [22] and even below 1 nm in TEMs [25] have been demonstrated. Moreover, there is a wide range of available precursor molecules with varying mechanical, electrical and magnetic properties [23]. Due to its excellent resolution and great versatility, FEBID has found applications in a wide range of research fields including nanoelectronics, nanooptics and nanolithography [23]. Moreover, in industry, FEBID, in combination with focused ion beam induced etching (FEBIE), has become the standard for mask repair and circuit editing [22].

In FEBID, materials are deposited inside an electron microscope with the help of a gas injection system (GIS). GIS needle is deployed close to the substrate supplying precursor molecules under low pressure. The molecules are diffused along the surface and physisorbed onto the substrate. The volatile organic ligands of the precursor are dissociated within the focus of the electron beam, inducing deposition only in a well defined region. It is worth noting that dissociation can be induced by primary, secondary or backscattered electrons. However, in most cases, it is dominated by secondary electrons [23].

Patterns are formed by beam scanning in a raster fashion, settling on given points for a specified "dwell" time. In addition, by reducing the distance between the dwell points and increasing the dwell time, the out of plane structures can be grown, making FEBID one of the few techniques that allow truly three-dimensional fabrication (Fig. 2). However, due to a dynamic interplay between electron-solid interactions and the spatial distribution of precursor molecules, vertical growth rate is not independent of the growth angle. In addition, it is sensitive to the temperature, pressure, and focus of the electron beam. This makes the relation between the given dwell time at each point and a resulting angle of growth θ highly non-trivial (Fig. 2d). Hence, even though simple architectures such as vertical or curving nanowires can be achieved with trial and error, consistent fabrication of complex 3D structures is not tractable with this approach [18].

In order to solve this problem, our collaborators J.D Fowlkes *et al.* have developed Monte Carlo-continuum simulations to model the growth of FEBID 3D nanostructures [18]. Moreover, they introduced a 3D computer-aided design (CAD) program, which generates beam movement parameters by both simulation and experiment (image in Appendix D). During this project, I contributed towards the development of their FEBID CAD software by testing it on structures of varying sizes and providing

feedback on features that should be implemented. The program, together with the theory behind it will soon be published.

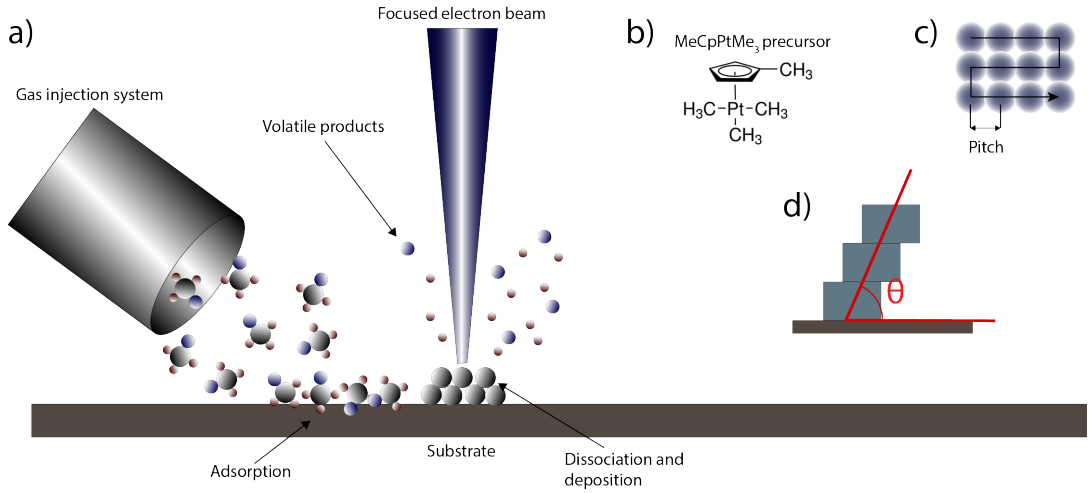

Figure 2: Focused electron induced deposition. (a) The illustration of FEBID growth: the precursor is supplied by GIS and physisorbed onto the substrate. The electron beam is dissociating the volatile products resulting in the material deposition; **(b)** Trimethyl (methylcyclopentadienyl) platinum(IV) molecule used as a precursor in our experiments; **(c)** Serpentine scanning pattern: the beam moves between points spaced by a set distance staying at each position for a given amount of dwell time; **(d)** Out of plane growth model: the pitch between the dwell points in the direction of out of plane growth is made to be small and the dwell times large. The angle θ is determined by the distance between dwell points, and the dwell time.

2.2 Fabrication

We use FEBID as a nanoprototyping tool for exploring the physics of domain wall motion in 3D structures and working towards electrical contacting of the magnetic nanowires. In all our experiments we used the FEI Helios NanoLab DualBeam electron microscope and Pt-C ($MeCpPt^{IV}Me_3$) precursor, building the structures at 30kV and 25pA under 35000x magnification on p-doped silicon substrates. The high voltage and low current were applied in order to reduce the area from which secondary electrons are emitted, improving the resolution. The FEBID structures were used as a scaffold for deposition of 50 nm thick layer of permalloy with an in-house built thermal evaporator. We use permalloy as a magnetic material for testing since it is simple to deposit, it is magnetically soft, has an in-plane magnetisation and a low anisotropy and magnetostriction.

I experimented with multiple FEBID designs to probe our level of control over the fabrication of complex structures (Fig. 3). However, for the purposes of this project, characterisation was restricted to simple straight nanowires . For the ease of magneto-optical detection (see Section 3), The NWs were fabricated under 30°to the substrate. Inter-layer strain due to different thermal expansion coefficients of permalloy and Pt-C scaffold tends to bend the structures during evaporation. Hence, two supporting legs were added to increase the structural stability. Moreover, I investigated the importance of smoothness of transition from the substrate to the main ramp by breaking it down into varying number of segments with incremental angles (see Fig. 3).

Since the conditions in the microscope chamber vary between sessions, at the start of each fabrication session we build calibration structures with different dwell times and fixed pixel point pitch in the direction of growth of 1 nm (Fig. 3). I wrote an edge detection program which extracts the angles the calibration structures form with the substrate from SEM pictures, giving us the dwell time versus segment angle dependence. Given a set of 3D points, and segments connecting them, the CAD program fits a curve to the calibration data and uses it to calculate the beam dwell times and scanning patterns required for fabrication.

Moreover, nucleation and proximity to the substrate have an effect on the rate of deposition, the

details of which are still under investigation. Hence, there are two paradigms when it comes to building the calibration data. To avoid substrate effects, we can first make a vertical segment, a method used in previous papers by J.D.Fowlkes et al [18, 19], or directly grow structures with a set dwell time (Fig. 3). Together with our collaborators, we are still investigating the exact effects via simulations, but we have found that, in practice, direct growth gives us better results. The plan for the future is to develop a program which would be able to take into account the proximity effects to evaluate dwell times, further improving the control over the building angle.

At large angles to the beam (or in other words, low dwell times) the segment angles become unreliable. This is due to the large slope of the calibration curve in this regime (Fig. 3): making small errors in calibration results in large angle errors. For this reason, our fabrication process was performed with the sample tilted by 30°, allowing us to build segments in the stable regime while maintaining the required 30°effective angle of the main ramp [17].

I constructed a library of Matlab functions which create an input for FEBID CAD in the form of points and segments from the given structure parameters. Moreover, in the later stages of the project, I further improved on the ideas from FEBID CAD by speeding up the calibration process, simplifying the UI and allowing for greater control over the beam scanning patterns and making easier the future implementation of proximity effect adjustments. At this stage, I have shown that the program is able to replicate the original FEBID CAD results in complex structures. However, further work is needed on interfacing with structure design programs the group has previously developed and implementing corrections to previously mentioned proximity effects.

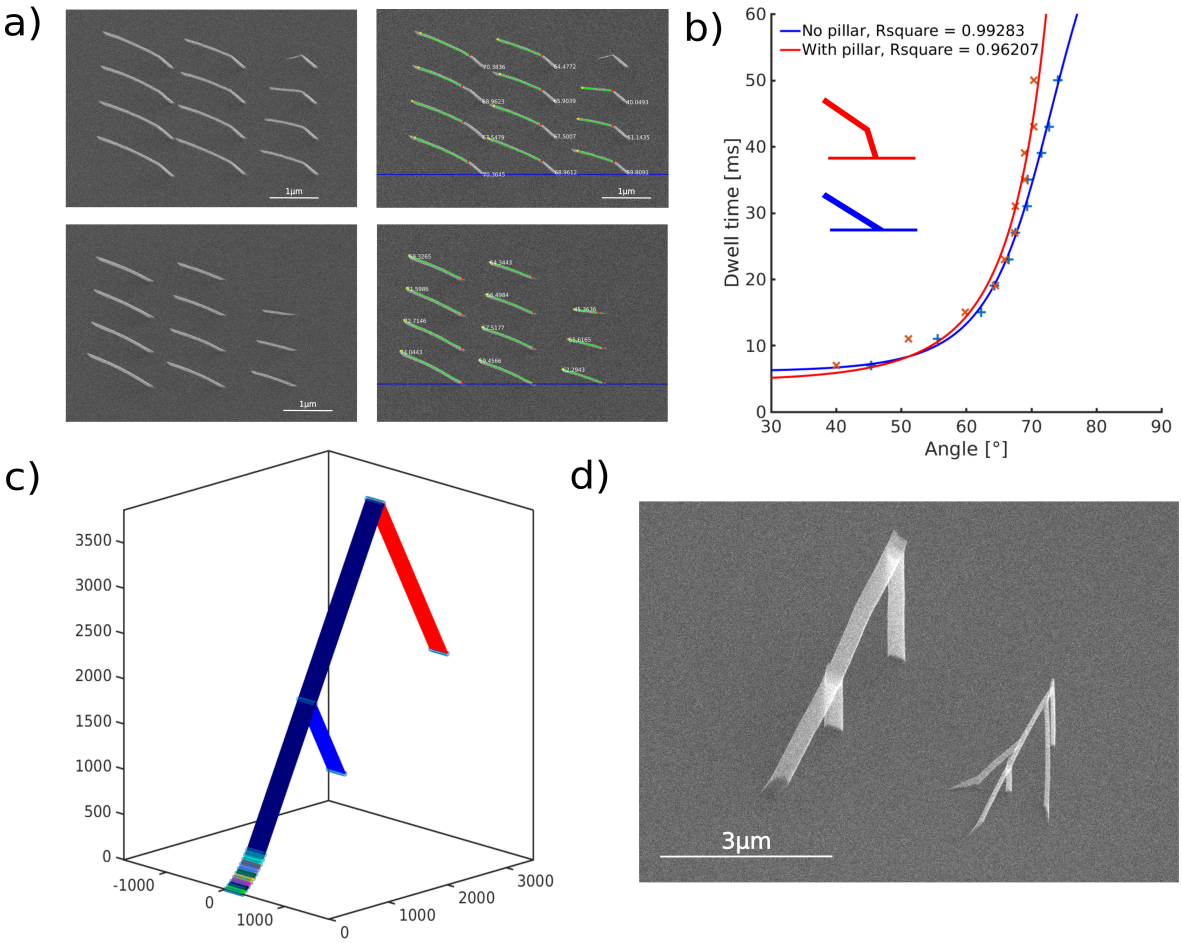

Figure 3: Making structures under FEBID (a) The two paradigms for making calibration structures: with initial pillar to avoid the substrate effects (above) and without (below). The initial pillar is under 60°to the substrate since we are growing under 30 °tilt. In both cases, the dwell times per point are increased between 3ms and 50ms with 4ms increments. Pitch in the direction of growth is always 1nm. Note that since the beam is moving too quickly, the structure with 3ms dwell time does not grow out of plane. To the right are the same pictures processed with my edge detection algorithm. The blue line is a reference used for angle calculation. **(b)** Plot of results of calibration structures from (a) and the associated fits. Note that the structures without the initial pillar need lower dwell times for a given angle. This could be caused by the faster vertical growth induced by the secondary electrons emitted by the surface or by the gradient in precursor concentration. **(c)** Model of the structure constructed by Matlab scripts. This particular structure is 4μm in projection and 300nm wide with 10 initial smoothing segments. The structure tilt is made to match the 30°substrate tilt. **(d)** SEM picture of two structures I built. Combining the calibration data with 3D models, we are able to reproducibly fabricate complex structures. Left is the structure modelled in (c). Right is one of the possible future designs for 4-probe electrical contacting

3 Magneto-optical characterisation

3.1 Overview

Magnetic characterisation of 3D nanostructures has been under investigation during the past years and presents a remarkable challenge [13, 4, 17]. Due to the high aspect ratios and no lateral separation between the structure and the substrate, the standard magnetometry and magnetic microscopy methods can not be applied. The methods such as PEEM, XMCD and Lorentz microscopy have been successfully used to image 3D magnetic textures with a resolution down to a nm scale [3]. However, these are specialist techniques, requiring expensive facilities and careful sample preparation.

In their recent work, the AFP group has developed dark-field Magneto-Optical Kerr Effect (MOKE) technique able to exploit the angle of 3D structures to separately image the substrate and the structure and thus characterise their switching mechanism [17]. In this configuration, two point detectors are positioned at different angles on an optical axis, corresponding to the angles of reflection from the structure and the film around it (see Fig. 4). The detector positioning allows for independent and simultaneous detection of MOKE signal from the two areas of interest. The experimental setup includes three sets of coils able to apply fields along any direction.

The main sources of uncertainty in the measurements are the angle between the substrate and the field plane, set to 33°± 3°and the distance between the substrate and coils. The biggest uncertainty of about 10% is in H_z field where there is just one magnetic coil acting as a monopole.

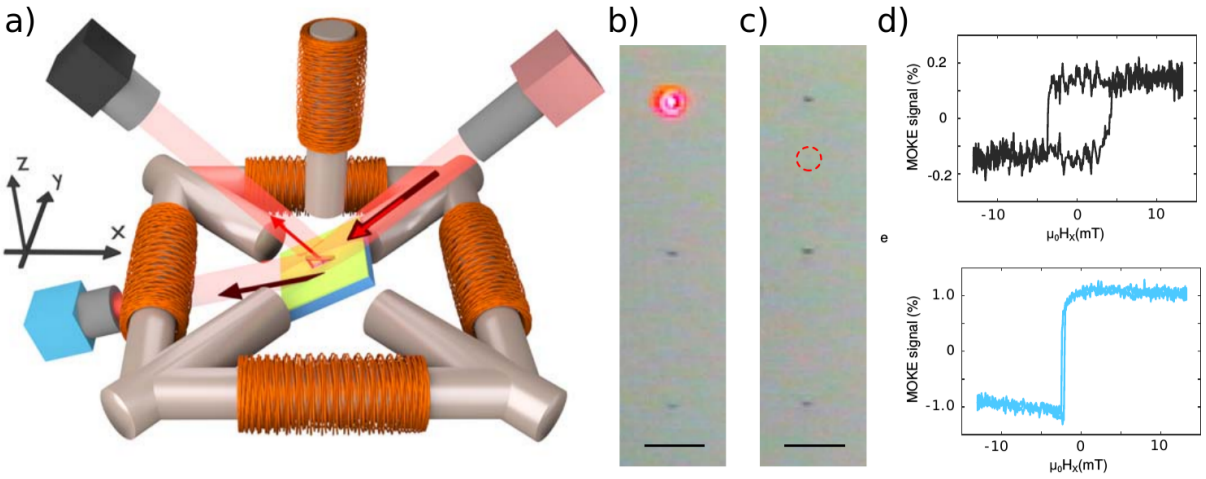

Figure 4: Dark field MOKE setup for characterisation of 3D nanowires. Adapted from [17] **(a)** The illustration of optical configuration and magnetic coils position. The laser path is positioned at 45°to the x-y plane. Substrate and structure signals are detected in the blue and black detectors respectively. the stage is positioned so that the structure is in the x-y plane of the fields while the substrate is at 33°± 3°, matching the NW inclination (see Sec. 2.2). . **(b), (c)** Optical images from CCD camera positioned at the same optical angle as the black detector. Laser light when aligned with the structure (b) and with the sample moved 20μm up, resulting in no laser light observed by the camera. Scale bars are 20μm. **(c)** examples of MOKE loops of the NW and film surrounding it

Since permalloy is a material with an in-plane magnetisation, the fields vertical to the deposited film have very little effect on the magnetisation of the thin films. It is important to note that in this configuration, the applied fields affect the structure and the substrate in different ways (see Fig. 5). The structure is aligned with the fields produced by the coil. However, as the substrate is tilted by an angle $\theta \approx 33°$around y axis, the projection of the fields to the plane of the substrate are:

$$
\begin{aligned}
H'_x &= H_x \cos\theta + H_z \sin\theta \\
H'_y &= H_y \\
H'_z &= -H_x \sin\theta + H_z \cos\theta
\end{aligned}
$$

Moreover, the nanostructure itself is often not perfectly flat and includes a smoothing ramp, as described before (see Section 2.2). The combination of the above makes the interpretation of isolated magnetic loops challenging. In our experiments, we get a full H_x-H_z switching fields dependence by oscillating the H_x field under a set of fixed H_z offsets. Matlab scripts made by D.S.Hernandez are then used to analyse hysteresis loops to find the locations of switching fields for each of the given z-offsets. The example of such a plot for a structure disconnected from the film from the group's recent paper [17] is given in Fig. 5. As there can not be DW injection from the film, and permalloy is an in-plane material, the interpretation is simplified in this case: the switching fields have no H_z dependence and the structure switches by nucleation at certain H_x. The film follows the same behaviour, but only with rotated fields H'_x and H'_z, and a significantly lower anisotropy.

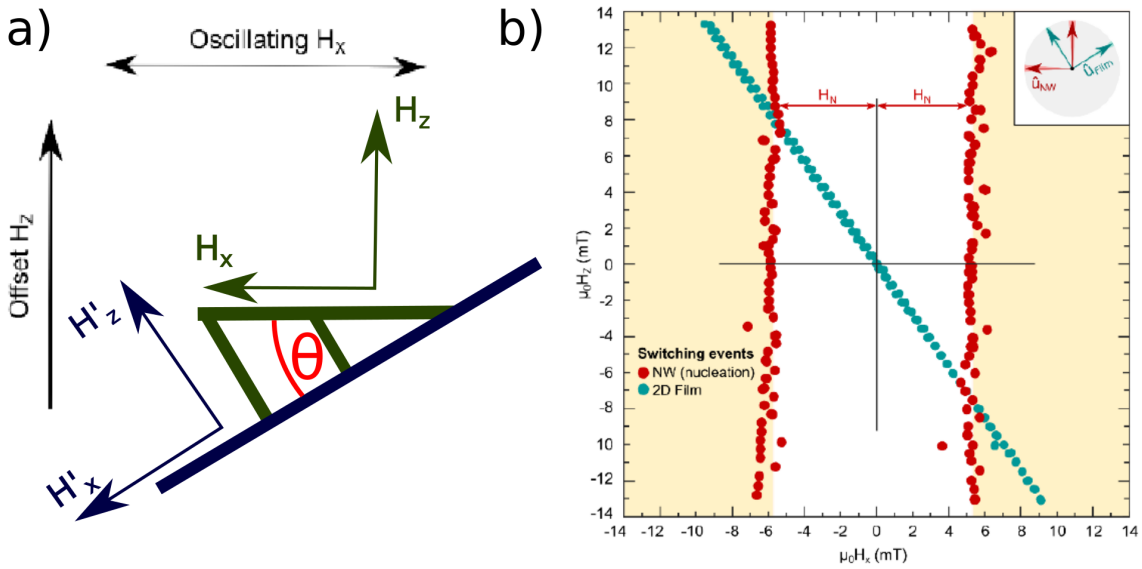

Figure 5: Field dependence of the film and the NW (a) Orientations of fields H_x and H_z to the film and NW, **(b)** Switching fields of the 2D film and a disconnected NW. Adapted from [17].

3.2 Characterisation of 3D structures using dark-field MOKE

I characterised the structures built under FEBID with the dark-field MOKE setup. To have a good noise-to-signal ratio, most characterised structures were made very large compared to the FEBID resolution: 300nm wide and 4μm long. However, we also tested the limits of resolution of the MOKE setup with several smaller structures, the smallest one being 80nm wide and 2μm, showing how this configuration can be used with great precision (see Appendix B).

The interconnected NWs show a much richer response of the switching fields than the disconnected ones. This includes asymmetric hysteresis loops and a switching diagram exhibiting three major switching regimes: propagation, transmission and nucleation. At small H_z offsets, due to a low anisotropy, the film around the structure switches first and acts as a source of DWs for the structure. DWs then propagate along the plane of the structure with defects acting as possible pinning sites. On the other hand, in the regime where the depinning happens at the interconnected area, the DWs are instantly transmitted along the structure once the barrier is overcome. Finally, as before, at high fields the DWs can be nucleated on the structure leading to switching before the injection happens.

In all cases, switching fields will form lines in the $H_x - H_z$ diagram which are perpendicular to the plane where the defining switching is happening. Thus, in an ideal NW, propagation and nucleation will show lines perpendicular to the x-y plane, while transmission, which is defined by the pinning at the connection, will be largely parallel to the substrate-defined line.

The above description of modes of switching has been demonstrated by D.S. Hernandez *et al.* via mumax micromagnetic simulations [17]. Furthermore, it is in compliance with the Kondorsky model for the domain wall propagation [26]. The angular dependence of the Kondorsky-type domain wall propagation is given by [27]:

$$H_{sw}(\theta) = \frac{H_0}{\cos(\theta)} \tag{1}$$

where θ is the angle of the applied field. The relationship holds for the straight segments in switching field plots for both propagation and transmission. H_0 can be determined by measuring the distance between the line of interest and a line parallel to it passing through the origin.

Moreover, it is worth noting that for the dimensions of our nanowires and the film thickness, we are expected to be in the vortex domain wall regime [5]. The smallest nanowire we measured, however, is approaching the regime for transverse wall generation which could be studied in the future for their different motion under externally applied magnetic fields [7]

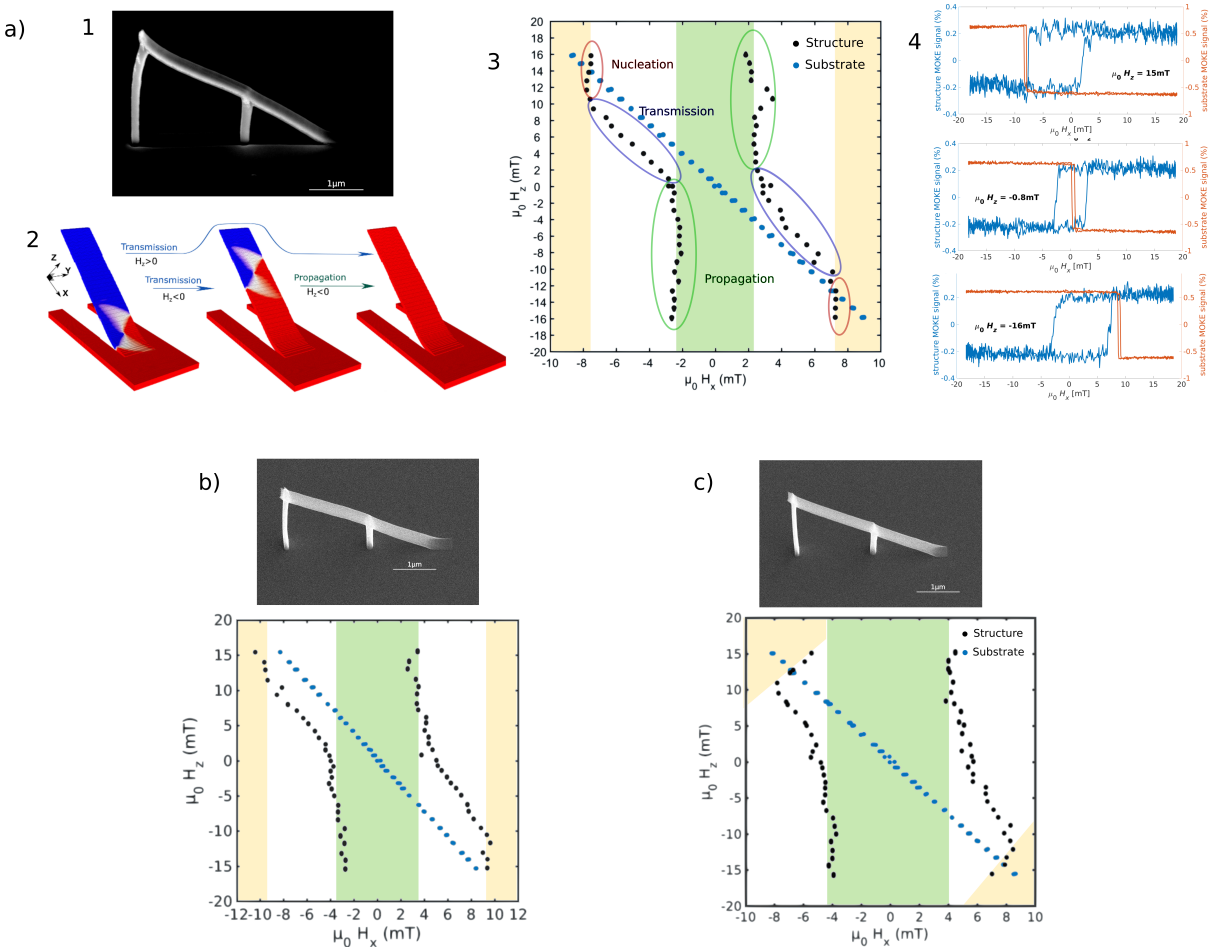

Figure 6: Switching fields for three different structures. The three nanostructures displayed in (a-c) are all 300nm wide and 4μm long (in projection to the substrate) built under 30°to the substrate, with a smoothing ramp split into varying number of segments over the first 500nm of length. **(a)** (1) SEM of a structure with smoothing ramp made up of 50 same-length segments of incremental angles (see Sec. 2.2). (2) Snapshots of simulations adapted from [17], showing domain wall motion in the three regimes. (3) Plot of switching fields of the structure with propagation, transmission and nucleation clearly defined. Injection fields for propagation are (2.3 ± 0.2) mT. Shaded regions are to guide the eye. (4) Examples of measured hysteresis loops for three different z-offsets. **(b)**NW with smoothing ramp split into 10 segments. The three regimes are still visible, but now with larger injection fields (3.5 ± 0.7mT). **(c)** NW with no smoothing ramp. Injection fields are (4.2 ± 0.5mT). In this case, nucleation switching fields are not aligned with the structure, but perpendicular to the surface telling us the orientation of the nucleation region. Hence, the region with defects which nucleate DWs is likely on the sides of the structure or at the very top. However, this is impossible to pinpoint without more advanced imaging techniques.

Using this description, we can define the barrier for propagation and nucleation. It is the half-width of the green region in plots in Fig. 6. In our measurements, we proved that we can controllably inject domain walls from the substrate plane onto the 3D structures, with the potential barrier for DW injection largely defined by the smoothness of the transition region.

As in this project, the main interest was the injection and propagation of DWs, I have not used the H_y fields. However, in their paper, D.S. Hernandez *et al.* have demonstrated that applying a large H_y offset can act as a gate to the DW injection. In the future, a further characterisation of the whole process with PEEM and STXM using synchrotron facilities in Soleil, France is planned. Moreover, the effects of different widths and FEBID scanning strategies on the DW motion will be investigated in a systematic way.

4 Top contact fabrication

4.1 Parylene

Post-processing of out-of-plane nanowires is made difficult by their sensitivity to standard lithography techniques. Processes such as resist spinning, sonication and lift-off have a high chance of breaking or seriously deforming the devices. S. Baig from the Joyce group has developed a fabrication process using parylene C to produce free standing vertically aligned nanowire-polymer thin films [20]. In this project, I worked on optimising this process in order to create an optically transparent top contact for 3D magnetic nanostructures.

Parylene C is a π-conjugated polymer from the family of "Parylenes" based on chemical structures known as para-xylenes. In our experiments, we use parylene C for nanowire encapsulation due to its wide availability, high deposition rates ($\sim 5\mu$m/hour [28]), compared to other parylenes and optical clarity ($\sim$99% visible light transmission [29]).

Parylene C polymerises through a free radical addition mechanism (see Fig. 7) and is deposited via the Gorham process [30]. The precursors are available as a dimer, which is vaporised at 120°C and cracked at 690°C to form a highly reactive diradical species, acting as the initiator, which via free radical addition forms polymetric parylene C. The coating process is extremely conformal due to its deposition in the vapour phase and the reactivity of the diradical species, making it to completely encapsulate the nanowires. The thickness of coating is proportional to the amount of precursor (see Fig. 8), allowing for fine control over the deposition process.

In addition, parylene offers several advantages that can be exploited in the future work. Firstly, it stabilises the encapsulated nanowires, making further processing significantly less likely to induce damage. This is allowing for standard lithography methods to be implemented on the top surface. Furthermore, it can be easily cut and peeled from the substrate in one piece, opening a path towards flexible devices, an application being explored by the Joyce group.

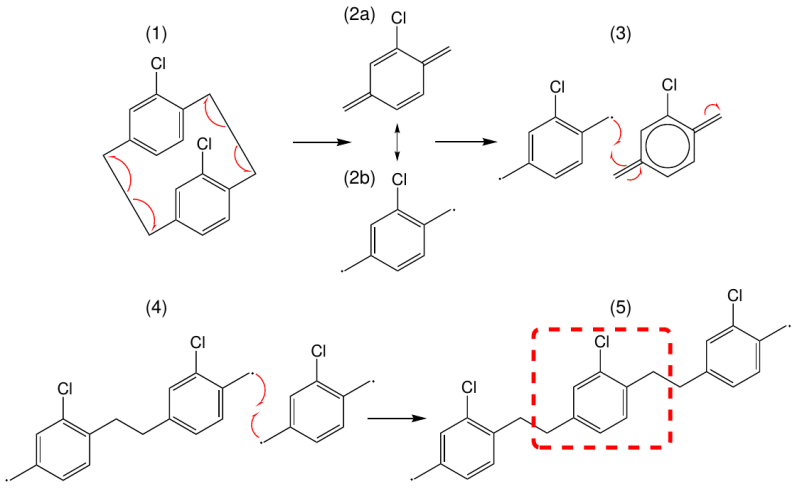

Figure 7: Parylene polymerisation The Parylene C dimer precursor is vaporised and cracked (1) to form a diradical species (2a) and cyclo-alkene resonant form (2b). Polymerisation takes place. (3) shows one pathway, where the diradical reacts with the cyclo-alkene species to produce another radical species. (4) shows an alternative pathway where two diradicals react to form a single bond between the aliphatic substituents. The reaction continues and forms polymeric Parylene C, outlined in red and shown as a repeating unit (5). Adapted from [20]

4.2 Top contact fabrication

The top contact is fabricated in 4 steps (see Fig. 8). Firstly, we cover the nanowires in parylene film with Labcoter 2 evaporator using the Gorham process. Since the structures we fabricated are about 2.3μm high, we deposited a 3μm thick layer of parylene, corresponding to 2.1g of Parylene C dimer. The sample is then etched with oxygen plasma Reactive Ion Etching (RIE) using the Philips RIE, so that only the tips of the structure stick out of the layer.

Initially, we used the parameters optimised by S.Baig for nanowires on InP substrates: 300W, 50sccm O_2 flow rate, with base pressure of 150mTorr for 2 minutes. The etched sample is then sputter coated with a 100nm thick layer of indium tin oxide (ITO). The optical transparency of ITO should allow us to optically probe the magnetic properties of contacted structures, simultaneously performing optical and electrical magnetic measurements. The sketch of the whole process can be seen in Fig. 8. Similar process has been employed previously by A.C.E Chia and R.R.LaPierre for top contacting of arrays of vertical semiconductor nanowires [31].

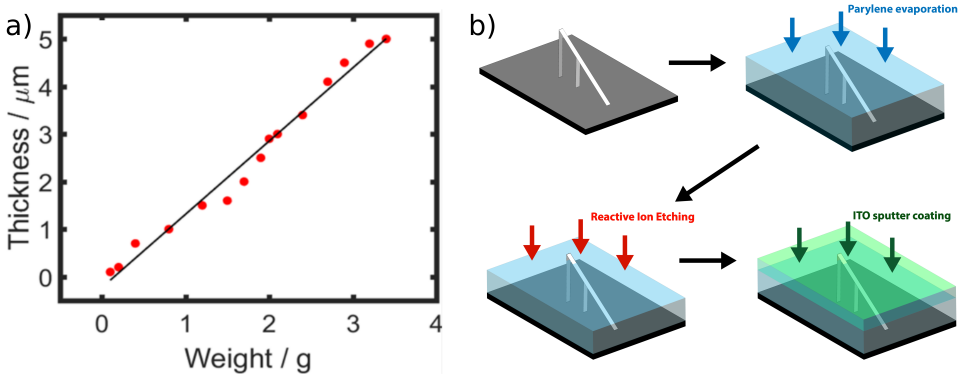

Figure 8: Top contact fabrication (a) Linear dependence of the parylene film thickness against the amount of polymer dimer used. Adapted from [20]. **(b)** Steps of the top contact fabrication process: parylene deposition, reactive ion etching via oxygen plasma, ITO sputter coating.

However, initial attempts of forming the contact resulted in unsatisfactory results. Firstly, due to the conformal nature of deposition, before RIE etching there is a parylene "bubble" which forms above the structure. This has been expected due to the similar results from S. Baig on her semiconducting nanowires [20]. I found that even though I was able to measure the substrate film, the refraction of light on the bubble surface resulted in too much noise for reliable measurements of the structure hysteresis loops.

According to the S.Baig results, RIE under high power can flatten the bubble. However, we noticed that etching introduces surface roughness. Moreover, this is further exasperated by the material being redeposited during the etching process, resulting in a very uneven surface (Fig. 9d). The combination of the above effects introduced a significant amount of laser scattering during MOKE characterisation. This led to the film signal dominating in both detectors (See 3), rendering us unable to perform measurements on nanowires under parylene without further optimisation.

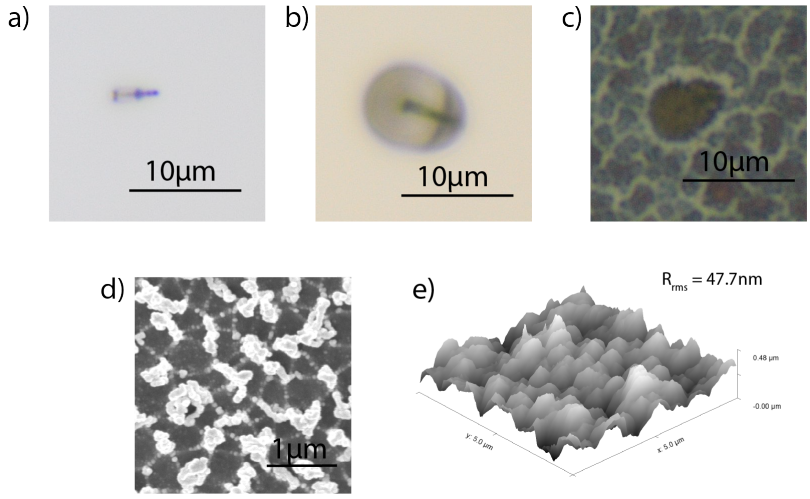

Figure 9: Roughness in parylene (a)-(c) Optical microscopy images of the nanowires with no parylene, after parylene evaporation and after finishing the top-contact process respectively. In (b), the parylene bubble can be seen around the structure while in (b) the image is dominated by the roughness induced by RIE. **(d)** SEM image of the surface of parylene after RIE and ITO deposition showing the effects of redeposition. No MOKE measurements were successfully performed on these structures due to the signal in both detectors being dominated by the film. (e) AFM image of the surface of the same sample with RMS roughness value.

4.3 RIE optimisation

To minimise the roughness of the etched parylene layer, I optimised the etching parameters of the RIE. All experiments were performed on p-doped Si substrates with parylene deposited from 2.1g of the precursor (8). This would correspond to 3μm thick layers according to Fig. 8a. However, during the optimisation stage, the parylene coater was in need of a thorough cleaning due to residue parylene in the precursor loading chamber, resulting in layers thicker than expected (see Appendix A).

In the Philips RIE I used, etching power, time, oxygen flow and working pressure can be adjusted. Base pressure is set by the machine and is about 50mTorr. We decided to keep the working pressure constant at 150mTorr, which is a standard for most processes the machine is used for, and optimised the remaining: power, time and oxygen flow.

Before starting the etching process, the chamber is cleaned with a 5 minute etching cycle at full power (300W) with 50sccm oxygen flow to remove any contaminants from the previous samples. In order to help remove the redeposited material, all samples were washed in acetone for 30 seconds and then dried on a hot plate at 40°for 2 minutes. It is important to note that this had no effect on the non-etched layer. Parylenes, once deposited are very stable and are insoluble in all common solvents at room temperature. In order to remove it, parylene C needs to be dissolved in high boiling liquids, such as I -chloronaphthalene or benzoyl benzoate at temperatures above 150°C [32].

To investigate the influence of each of the parameters, an intermediate reference set was taken: 150W, 50sccm of O_2, and 2 minutes. Each of the parameters was changed separately to be significantly higher or smaller than the reference, while keeping the others fixed. The root mean square (RMS) roughness of each of the etched samples, together with two parylene samples which had no post processing done on them, was measured using the MFP-3D AFM system in tapping mode on 5μm x 5μm scale. Moreover, the total thickness of the etched layer was measured with Dektak profilometer which has ∼50nm vertical resolution. The full measurement I took are in Appendix A.

Firstly, it was found that the evaporated parylene layer is very smooth, with RMS of 4.6nm. In the etched samples, the RMS roughness was strongly anti-correlated with the final layer thickness (Fig. 10), making both longer times and higher etching power increase the roughness. However, I found that a high gas flow reduces the roughness, with little change in the etching rate. Moreover, it is important to note that just by washing the samples in acetone, the RMS roughness of the intermediate-parameter sample was reduced from 47.7nm to 26.9nm. Also, our p-doped Si samples show a very high etching rate when compared to InP substrates previously used by S.Baig. The combination of the above explains our poor initial results.

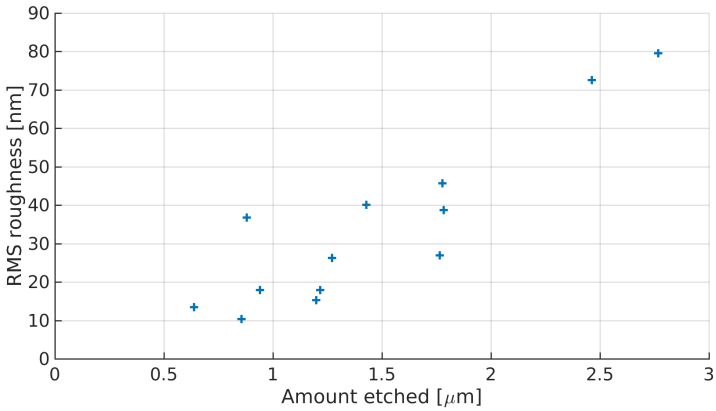

Figure 10: RIE induced roughness The amount etched measured by a profilometer with 50nm precision compared to AFM surface roughness measurements on samples with varying etching parameters. Full table in Appendix A

The sample with the smoothest final layer was the one where we etched for 1 minute with 100W and O_2 flow of 100sccm. In this sample, the amount etchet was (850±50)nm, while maintaining RMS of less than 11nm. Since the consistency of RIE etching has not been tested, we allow for up to 30% error in both numbers, while still achieving satisfactory results. These etching parameters were applied on one of the samples with FEBID-built magnetic nanowires 11. Although we could still see the bubble over the structure, we were now able to perform MOKE measurements showing significant improvement. However, signal-to-noise ratio was lower than before the polymer deposition.

To improve on this, further optimisation is needed. Etching larger amounts of materials has been shown to introduce more surface roughness, but at the same time is expected to flatten the bubble. Therefore, the next step in the optimisation will be to correlate the two competing effects to improve signal-to-noise ratio. Since I was unable to do so during the duration of this project due to time constraints, this will be done at the start of the PhD project.

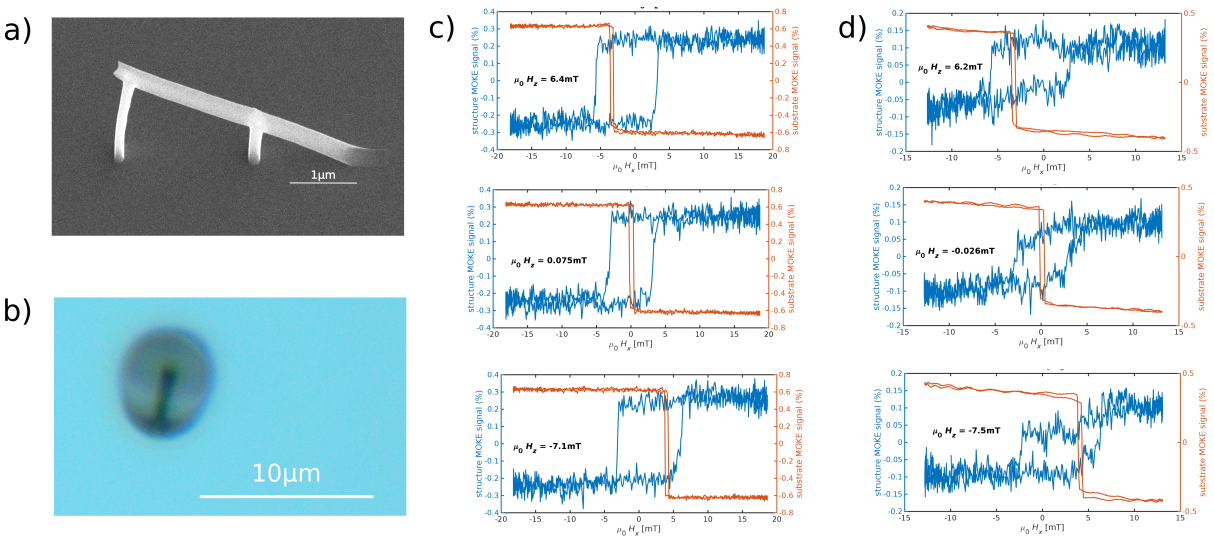

Figure 11: MOKE measurements through parylene. (a) SEM image of the measured structure. The structure is of the same type as Fig. 6b: 300nm wide, 4μm long and with 10-stage smoothing ramp. **b** Optical microscopy image after parylene deposition and RIE. The parylene bubble is still visible, but it is almost half the size as the one in Fig. 9 . The MOKE loops before parylene **(c)**, and after the parylene and optimised RIE process **(d)** for three different H_z offsets. The loops in (d) have a lower signal to noise ration, but the switching fields are clearly visible and agree with (c).

5 Conclusion and further work

Development of advanced nanofabrication and characterisation methods is required for the advance of 3D spintronics. During this midi project, I have tested and improved on the CAD software designed for reproducibly building complex 3D nanostructures under FEBID with a great level of control. I investigated the surface proximity effects for different calibration paradigms and applied them to my designs. The built structures were characterised using dark-field MOKE, testing the limits of resolution, and proving that domain walls can controllably be transmitted through the built nanostructures. In addition, the injection fields were compared with the smoothness of transition from the substrate, showing that smoother transitions result in lower injection fields.

Moreover, I worked towards creating an optically transparent top contact for out-of-plane nanowires. I worked on optimisation of the etching process by measuring the deposited layer thickness and root mean square roughness. A set of parameters optimised for surface roughness was applied and magneto-optical measurements through the resulting parylene layer have been demonstrated.

The project has created a strong basis for the start of the PhD project which will explore the electrical effects on the domain walls in 3D nanowires. Firstly, I plan to finish interfacing the FEBID programs with the programs previously built by the group allowing us to quickly design and build nanostructures of arbitrary geometry. In particular, I plan to build structures with curvature, such as spirals or arches and investigate the chirality effects on the DW propagation. Secondly, I will work on finishing the development of the parylene process for building an optically transparent top contact on out-of-plane nanowires. This will allow us to perform both optical and electrical measurements on 3D nanostructures, going towards experimenting with influence of different geometries on the magneto-electrical effects and domain wall motion under both external fields, and current pulses. In addition, detailed characterisation of the DW topology and its motion in 3D structures will be done in the synchrotron facilities using PEEM and STXM.

References

[1] D. A. Allwood, G. Xiong, C. C. Faulkner, D. Atkinson, D. Petit, and R. P. Cowburn. Magnetic Domain-Wall Logic. *Science*, 309(5741):1688–1692, September 2005.

[2] Stuart Parkin and See-Hun Yang. Memory on the racetrack. *Nat Nano*, 10(3):195–198, March 2015.

[3] Amalio Fernández-Pacheco, Robert Streubel, Olivier Fruchart, Riccardo Hertel, Peter Fischer, and Russell P. Cowburn. Three-dimensional nanomagnetism. *Nature Communications*, 8, June 2017.

[4] Robert Streubel, Peter Fischer, Florian Kronast, Volodymyr P. Kravchuk, Denis D. Sheka, Yuri Gaididei, Oliver G. Schmidt, and Denys Makarov. Magnetism in curved geometries. *J. Phys. D: Appl. Phys.*, 49(36):363001, 2016.

[5] Yoshinobu Nakatani, André Thiaville, and Jacques Miltat. Head-to-head domain walls in soft nano-strips: a refined phase diagram. *Journal of Magnetism and Magnetic Materials*, 290:750–753, April 2005.

[6] R. Sbiaa, H. Meng, and S. N. Piramanayagam. Materials with perpendicular magnetic anisotropy for magnetic random access memory. *Phys. Status Solidi RRL*, 5(12):413–419, December 2011.

[7] Dorothée Petit, Ana-Vanessa Jausovec, Huang T. Zeng, Emma Lewis, Liam O'Brien, Dan Read, and Russell P. Cowburn. Mechanism for domain wall pinning and potential landscape modification by artificially patterned traps in ferromagnetic nanowires. *Phys. Rev. B*, 79(21):214405, June 2009.

[8] J. Vogel, M. Bonfim, N. Rougemaille, O. Boulle, I. M. Miron, S. Auffret, B. Rodmacq, G. Gaudin, J. C. Cezar, F. Sirotti, and S. Pizzini. Direct Observation of Massless Domain Wall Dynamics in Nanostripes with Perpendicular Magnetic Anisotropy. *Phys. Rev. Lett.*, 108(24):247202, June 2012.

[9] Satoru Emori, Uwe Bauer, Sung-Min Ahn, Eduardo Martinez, and Geoffrey S. D. Beach. Current-driven dynamics of chiral ferromagnetic domain walls. *Nat Mater*, 12(7):611–616, July 2013.

[10] A. N. Bogdanov and U. K. Rößler. Chiral Symmetry Breaking in Magnetic Thin Films and Multilayers. *Phys. Rev. Lett.*, 87(3):037203, June 2001.

[11] Riccardo Hertel. Curvature-induced magnetochirality. *SPIN*, 03(03):1340009, September 2013.

[12] Wanjun Jiang, Pramey Upadhyaya, Wei Zhang, Guoqiang Yu, M. Benjamin Jungfleisch, Frank Y. Fradin, John E. Pearson, Yaroslav Tserkovnyak, Kang L. Wang, Olle Heinonen, Suzanne G. E. te Velthuis, and Axel Hoffmann. Magnetism. Blowing magnetic skyrmion bubbles. *Science*, 349(6245):283–286, July 2015.

[13] Amalio Fernández-Pacheco, Luis Serrano-Ramón, Jan M. Michalik, M. Ricardo Ibarra, José M. De Teresa, Liam O'Brien, Dorothée Petit, Jihyun Lee, and Russell P. Cowburn. Three dimensional magnetic nanowires grown by focused electron-beam induced deposition. *Sci Rep*, 3, March 2013.

[14] Javier Pablo-Navarro, Dédalo Sanz-Hernández, César Magén, Amalio Fernández-Pacheco, and José María de Teresa. Tuning shape, composition and magnetization of 3d cobalt nanowires grown by focused electron beam induced deposition (FEBID). *J. Phys. D: Appl. Phys.*, 50(18):18LT01, 2017.

[15] Reinoud Lavrijsen, Ji-Hyun Lee, Amalio Fernández-Pacheco, Dorothée C. M. C. Petit, Rhodri Mansell, and Russell P. Cowburn. Magnetic ratchet for three-dimensional spintronic memory and logic. *Nature*, 493(7434):647–650, January 2013.

[16] Amalio Fernández-Pacheco, Nina-Juliane Steinke, Dishant Mahendru, Alexander Welbourne, Rhodri Mansell, Shin L. Chin, Dorothée Petit, JiHyun Lee, Robert Dalgliesh, Sean Langridge, and Russell P. Cowburn. Magnetic State of Multilayered Synthetic Antiferromagnets during Soliton Nucleation and Propagation for Vertical Data Transfer. *Adv. Mater. Interfaces*, 3(15), August 2016.

[17] Dédalo Sanz-Hernández, Ruben F. Hamans, Jung-Wei Liao, Alexander Welbourne, Reinoud Lavrijsen, and Amalio Fernández-Pacheco. Fabrication, detection and operation of a three-dimensional nanomagnetic conduit. *arXiv:1706.03710*, June 2017. arXiv: 1706.03710.

[18] Jason D. Fowlkes, Robert Winkler, Brett B. Lewis, Michael G. Stanford, Harald Plank, and Philip D. Rack. Simulation-Guided 3d Nanomanufacturing via Focused Electron Beam Induced Deposition. *ACS Nano*, 2016.

[19] Brett B Lewis, Robert Winkler, Xiahan Sang, Pushpa R Pudasaini, Michael G Stanford, Harald Plank, Raymond R Unocic, Jason D Fowlkes, and Philip D Rack. 3d Nanoprinting via laser-assisted electron beam induced deposition: growth kinetics, enhanced purity, and electrical resistivity. *Beilstein J Nanotechnol*, 8:801–812, April 2017.

[20] S. Baig. *Flexible and substrate-free optoelectronic devices based on III-V semiconductor nanowires, (Unpublished doctoral thesis)*. PhD thesis, University of Cambridge, 2017.

[21] Hannah J. Joyce, Jessica L. Boland, Christopher L. Davies, Sarwat A. Baig, and Michael B. Johnston. A review of the electrical properties of semiconductor nanowires: insights gained from terahertz conductivity spectroscopy. *Semicond. Sci. Technol.*, 31(10):103003, 2016.

[22] Michael Huth, Fabrizio Porrati, Christian Schwalb, Marcel Winhold, Roland Sachser, Maja Dukic, Jonathan Adams, and Georg Fantner. Focused electron beam induced deposition: A perspective. *Beilstein Journal of Nanotechnology*, 3:597–619, August 2012.

[23] Ivo Utke, Patrik Hoffmann, and John Melngailis. Gas-assisted focused electron beam and ion beam processing and fabrication. *Journal of Vacuum Science & Technology B: Microelectronics and Nanometer Structures Processing, Measurement, and Phenomena*, 26(4):1197–1276, 2008.

[24] V. Friedli and I. Utke. Optimized molecule supply from nozzle-based gas injection systems for focused electron and and ion-beam induced deposition and etching simulation and experiment. *IOP Science*, 2017.

[25] W. F. van Dorp, C. W. Hagen, P. A. Crozier, and P. Kruit. Growth behavior near the ultimate resolution of nanometer-scale focused electron beam-induced deposition. *Nanotechnology*, 19(22):225305, 2008.

[26] E. Kondorsky. On hysteresis of ferromagnetics. (2):161–181, 1940.

[27] E. Stoner. The demagnetizing factors for ellipsoids. (36):803–821, 1945.

[28] Joel Jean, Annie Wang, and Vladimir Bulović. In situ vapor-deposited parylene substrates for ultra-thin, lightweight organic solar cells. *Organic Electronics*, 31:120–126, April 2016.

[29] Y.S. Jeong, B. Ratier, A. Moliton, and L. Guyard. UV–visible and infrared characterization of poly(p-

xylylene) films for waveguide applications and OLED encapsulation. 127:189–193, 2002.

[30] William F. Gorham. A New, General Synthetic Method for the Preparation of Linear Poly-p-xylylenes. *Journal of Polymer Science*, 4:3027–3039, 1966.

[31] A. C. E. Chia and R. R. LaPierre. Contact planarization of ensemble nanowires. *Nanotechnology*, 22(24):245304, 2011.

[32] Solvent Resistance of Parylenes C,N,D.

Appendices

A RIE optimisation data

Sample	Etching time [min]	Gas flow [sccm]	Power [W]	RMS roughness [nm]	Thickness [µm]
1	1	50	150	15.2	3.6
2	4	50	150	79.6	2.1
3	2	25	150	40.1	3.4
4	2	100	150	26.2	3.6
5	2	50	100	17.9	3.9
6	2	50	300	72.5	2.4
7	2	50	150	26.9	3.1
8	2	50	100	17.9	3.6
9	2	50	150	45.6	3.1
10	1	100	100	10.4	4.0
11	1	25	100	13.4	4.2
12	4	100	100	36.8	4.0
13	1	100	300	38.7	3.1

Figure 12: Measurements of root mean square roughness and thickness of the parylene layer after etching with varying parameters: etching time, O_2 gas flow, and etching power. A reference sample with no etching had RMS roughness of 4.6nm with the thickness of 4.8μm

B Smallest measured structure

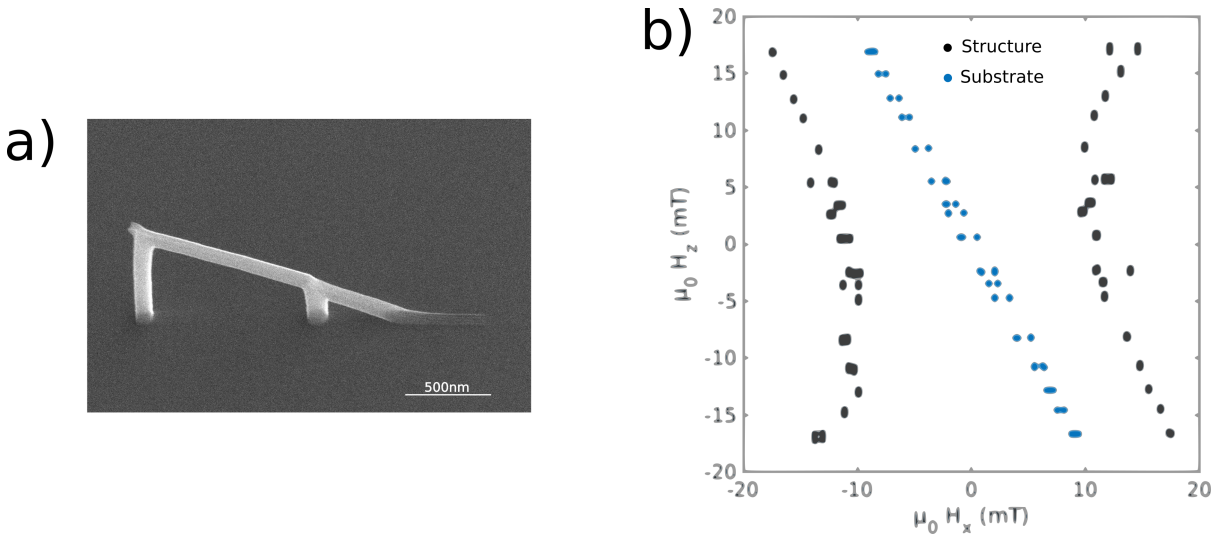

Figure 13: (a) SEM and (b) switching fields of the smallest structure measured to date. The structure is 2μm long and 80nm wide. Transmission, propagation and nucleation are not well defined, most likely due to the visible growth defect at the inner supporting leg.

C Moke setup

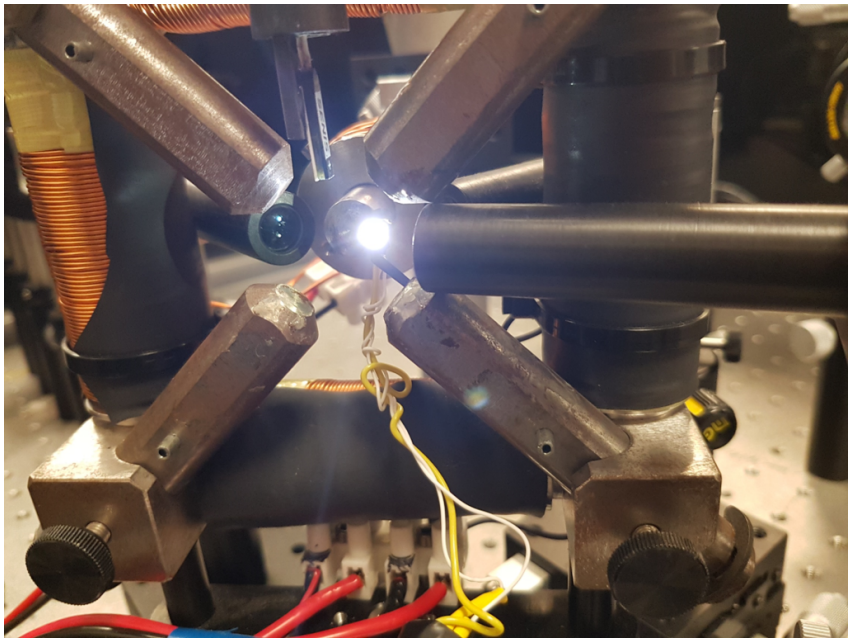

Figure 14: Picture of the dark-field MOKE setup with a mounted LED. The surface-mount LED with controllable brightness was my addition which made sample alignment easier and significantly faster.

D FEBID CAD

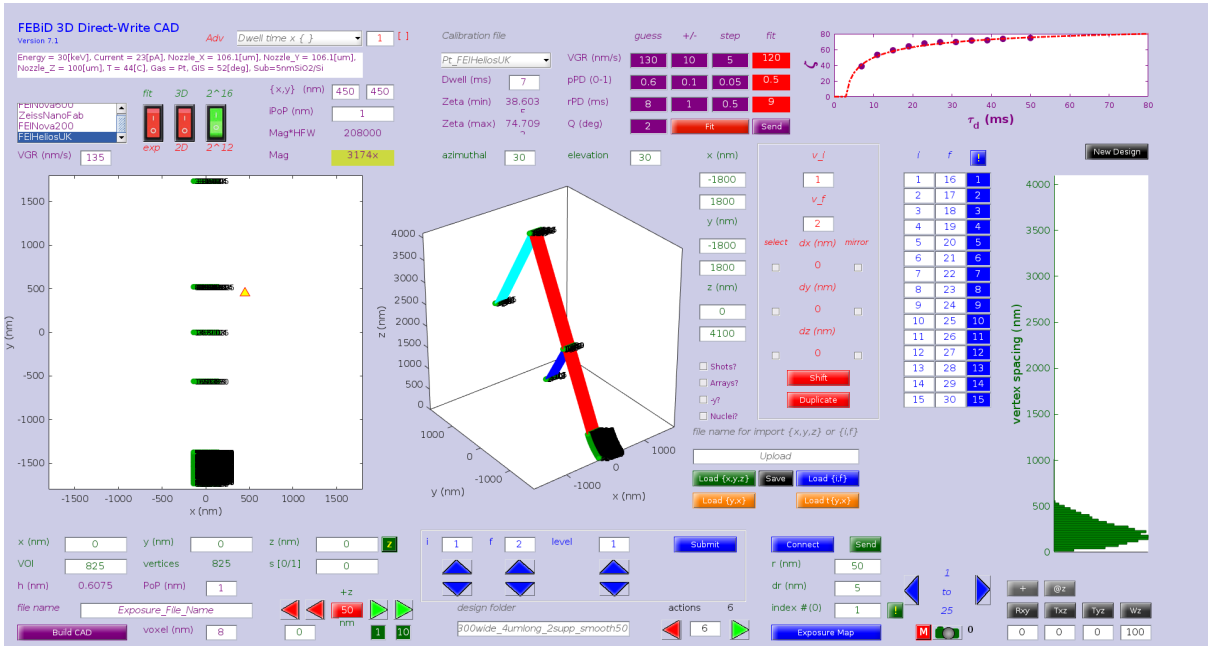

Figure 15: Snapshot of FEBID CAD software developed by our collaborator J.D.Fowlkes for creation of beam scanning patterns for FEBID. The documentation and the source code will soon be published.